JOURNAL OF PROPULSION AND POWER
Vol. 18, No. 6, November–December 2002

# Technical Notes

*TECHNICAL NOTES are short manuscripts describing new developments or important results of a preliminary nature. These Notes cannot exceed 6 manuscript pages and 3 figures; a page of text may be substituted for a figure and vice versa. After informal review by the editors, they may be published within a few months of the date of receipt. Style requirements are the same as for regular contributions (see inside back cover).*

## Effects of End Wall Geometry and Stacking on Supersonic Turbine Performance

Daniel J. Dorney* and Lisa W. Griffin†
*NASA Marshall Space Flight Center, Huntsville, Alabama 35812*
Frank W. Huber‡
*Riverbend Design Services, Palm Beach Gardens, Florida 33418*
and
Douglas L. Sondak§
*Boston University, Boston, Massachusetts 02215*

### Introduction

MODERN high-work turbines can be compact, transonic, supersonic, counter rotating, and can use a dense drive gas. The vast majority of modern rocket turbine designs fall into these categories. These turbines are often characterized by large amounts of flow unsteadiness. The flow unsteadiness can have a major impact on turbine performance and durability. For example, the Space Transportation Main Engine fuel turbine, a high-work transonic design, was found to have an unsteady interrow shock, which reduced efficiency by two points and increased dynamic loading by 24%. The Revolutionary Reusable Technology Turbopump (RRTT), which uses full flow oxygen for its drive gas, was found to shed vortices with such energy as to raise serious blade durability concerns. In both cases the sources of the problems were uncovered before turbopump testing with the application of unsteady computational fluid dynamics (CFD) to the designs. In the case of the RRTT and the Alternate Turbopump Development turbines, the unsteady CFD codes were used not just to identify problems, but to guide designs that mitigate problems caused by unsteadiness. Using unsteady flow analyses as a part of the design process has led to turbine designs with higher performance and fewer dynamics problems.

Recently, CFD has been used in the design a two-stage supersonic turbine that will be tested experimentally during 2002 (Refs. 1–3). Simulations, including mean-line, two-dimensional CFD, and three-dimensional CFD analyses in conjunction with optimization techniques, were used to design both the flowpath and the airfoil geometries. During the course of this work, a large separated flow region was detected on the hub end wall between the first-stage vane and the first-stage rotor.

Two methods are commonly used to control the secondary/separated flows (and associated losses) in supersonic turbines: end-wall contouring and airfoil stacking. In the current investigation the flow path between the first-stage vanes and rotors and the stacking of the first-stage vanes were varied in an effort to improve turbine performance. The geometric variations have been studied by performing a series of unsteady three-dimensional numerical simulations for the two-stage turbine.

### Numerical Algorithm

The governing equations considered in this study are the time-dependent, three-dimensional Reynolds-averaged Navier–Stokes equations. To extend the equations of motion to turbulent flows, an eddy viscosity formulation is used. The turbulent viscosity is calculated using a two-layer algebraic turbulence model.

A time-marching, implicit, finite difference scheme has been used, which is third-order spatially accurate and second-order temporally accurate. The inviscid fluxes are discretized using a third-order upwind-biased scheme. The viscous fluxes are calculated using standard central differences. An approximate-factorization technique is used to compute the time rate changes in the conserved variables. Newton subiterations are used at each global time step to increase stability and reduce linearization errors. For all cases investigated in this study, two Newton subiterations were performed at each time step. Message passing interface (MPI) and OpenMP Application Program Interface (APIs) have been used to parallelize the code to reduce the time for large-scale three-dimensional simulations.

The Navier–Stokes analysis uses O- and H-type zonal grids to discretize the flowfield and facilitate relative motion of the rotating components. The O-grids are body fitted to the surfaces of the airfoils and generated using an elliptic equation solution procedure. They are used to properly resolve the viscous flow in the blade passages and to facilitate the application of the algebraic turbulence model. The algebraically generated H-grids are used to discretize the remainder of the flowfield.

The computational analysis has been validated on several supersonic turbine geometries (e.g., Refs. 4 and 5).

### Geometry and Grids

The two-stage supersonic turbine configuration has 12 first-stage vanes, 30 first-stage rotors, 73 second-stage vanes, and 56 second-stage rotors. In the current effort a 15-vane/30-rotor/75-vane/60-rotor (1/2/5/4) airfoil approximation has been made. To keep the pitch-to-chord ratio (blockage) constant, the first-stage vanes were scaled by a factor of 12/15, the second-stage vanes were scaled by a factor of 73/75, and the second-stage rotors were scaled by a factor of 56/60. The tip clearance in the first- and second-stage rotors was set at the design value of approximately 2.0% of the respective rotor heights.

The grid densities (number of passages $\times\ i \times j \times k$) for the turbine simulations are presented in Table 1. The total number of grid points used to discretize the turbine was 4,139,957. The average

Received 4 January 2002; presented as Paper 2002-0078 at the 40th Aerospace Sciences Meeting and Exhibit, Reno, NV, 14–17 January 2002; revision received 22 June 2002; accepted for publication 3 July 2002. 

*Aerospace Engineer, Fluid Dynamics Analysis Branch. Associate Fellow AIAA.
†Team Leader, Fluid Dynamics Analysis Branch. Senior Member AIAA.
‡President. Senior Member AIAA.
§Senior Scientific Programmer, Office of Information Technology. Senior Member AIAA.

**Table 1 Grid dimensions for the two-stage turbine**

| Grid type | Vane-1 | Rotor-1 | Vane-2 | Rotor-2 |
|---|---|---|---|---|
| O | $1 \times 141 \times 31 \times 51$ | $2 \times 151 \times 21 \times 51$ | $5 \times 121 \times 31 \times 51$ | $4 \times 121 \times 31 \times 51$ |
| H | $1 \times 67 \times 41 \times 51$ | $2 \times 64 \times 41 \times 51$ | $5 \times 64 \times 41 \times 51$ | $4 \times 82 \times 41 \times 51$ |
| Tip | —— | $2 \times 151 \times 26 \times 7$ | —— | $4 \times 121 \times 16 \times 7$ |
| **Total points** | **363,018** | **646,054** | **1,525,625** | **1,505,260** |

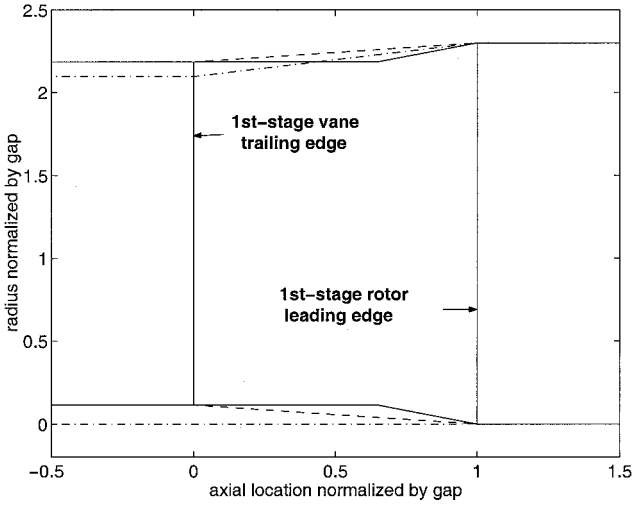


**Fig. 1 End-wall flowpath between first-stage vane and rotor: ——, case 1; – – –, case 2; - - - -, cases 3, 4.**

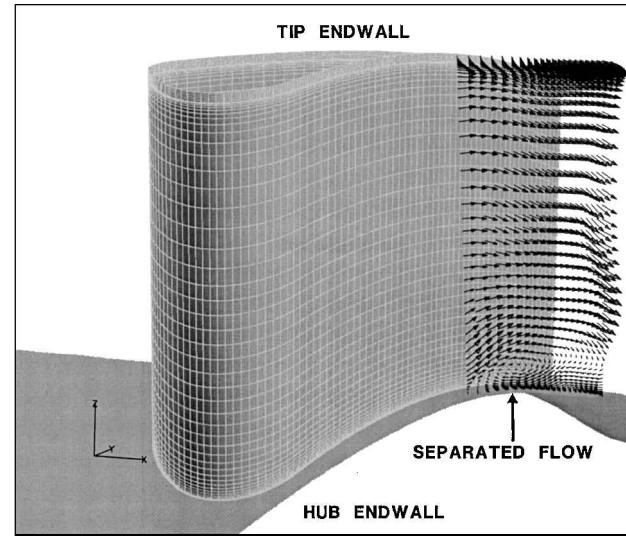


**Fig. 2 Time-averaged velocity vectors: vane-1—case 1.**

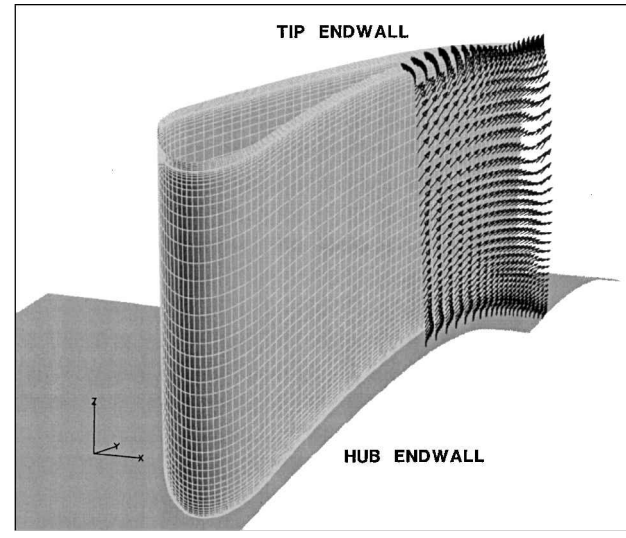


**Fig. 3 Time-averaged velocity vectors: vane-1—case 2.**

value of $y^+$, the nondimensional distance of the first grid line above the surface, was approximately 1.0 for the airfoil surfaces and 1.5 for the end-wall surfaces.

The simulations were run on 24 400-MHz R12000 processors of an SGI Origin2000. Each simulation was run for 15.0 global cycles (one complete rotor revolution) at 22,000 time steps per cycle. A global cycle is defined as the time it takes for the two first-stage rotor blades to pass by the first-stage vane airfoil. The value of 22,000 iterations per cycle was chosen to resolve all of the expected frequencies of interest. A time step required an average of 9.0 s CPU time on each of 24 processors. The time periodicity of the solutions was determined by interrogating pressure traces at points along the airfoil surfaces.

## Numerical Results

The two-stage turbine under consideration has a design inlet Mach number of $M_0 = 0.08$, an inlet total pressure of 15.4 MPa, and an inlet total temperature of approximately $T_0 = 1236$ K. The rotor rotates at $\Omega = 31{,}343$ rpm, the Reynolds number based on the inlet conditions and the rotor axial chord is approximately $1.2 \times 10^6$, and the ratio of the midspan exit static pressure to first-stage vane inlet total pressure is 0.1135. The operating fluid is hydrogen-rich steam, and the average ratio of specific heats is $\gamma = 1.3538$.

Four different simulations have been performed to determine the effects of end-wall shape and first-stage vane stacking on the performance of the two-stage turbine:

1) Case 1 represents the original turbine geometry based on previous work.[1–3] The radius of the inner diameter (ID) and outer diameter (OD) varies linearly from the nominal values in the first-stage vane passage to the final values in the rotor passage. The transition begins about $\frac{3}{4}$ of the way between the vane trailing edge and the rotor leading edge and concludes at the rotor leading edge (see Fig. 1).

2) Case 2 shows that the radius of the ID and OD vary linearly from the nominal values in the vane passage to the final values in the rotor passage beginning at the vane trailing edge and concluding at the rotor leading edge (see Fig. 1).

3) Case 3 shows that the radius of the ID is kept constant at the value used in the rotor. The radius of the OD varies linearly from the nominal value in the vane passage to the final value in the rotor passage beginning at the vane trailing edge and concluding at the rotor leading edge (see Fig. 1). In this case the height of the vane was increased to keep the vane flow area the same as in cases 1 and 2.

4) Case 4 reveals a flowpath that is identical to that used in case 3. The vane airfoils are stacked along the trailing edge instead of the center of gravity (as it was in cases 1, 2, and 3). Note, the restacking also gives the vane airfoils an inward radial lean.

Time-averaged velocity vectors in the first-stage vane passage in case 1 are shown in Fig. 2. The contours show a large region of separated flow extending from the hub to approximately 20% of the span. The axial extent of the region was confined to the area between the vane trailing edge and the rotor leading edge. It was initially theorized that the large separated flow region was being induced by the rapid expansion in the end-wall flowpath in case 1. Reducing the slope of the end wall in cases 2 and 3, however, did not significantly affect the size of the separated flow region. The next hypothesis was that stacking the vanes along the center of gravity causes the vane throat to point outward toward the shroud end wall, giving the flow a tendency to pull away from the hub end wall. In

particular, the stacking in cases 1–3 results in a radial flow angle of approximately 23 deg with respect to the axial direction. Restacking the vanes along a radial line connecting the trailing-edge points significantly reduced the size of the separated flow region (see Fig. 3).

Tables 2–5 contain the area- and time-averaged relative reference frame flow quantities at the inlet and exit of each blade row for all four cases. Area-averaged values were used in place of mass-averaged values because of the large-scale separation. The calculated value of the reaction is based on the static pressures in each blade row. Some of the relevant information that can be deduced from these tables includes the following:

1) Reducing the size of the separated flow region resulted in an increase in the average vane exit Mach number to 1.37, as compared with 1.17 in case 1 and 1.15 in cases 2 and 3.

2) Reducing the size of the separated flow region in case 4 gives a significant increase in turbine efficiency. The increase was in excess of seven points compared to case 3 and nearly six points compared to case 1. A more detailed comparison of cases 1 and 4 is presented next.

**Table 2 Turbine time-averaged relative flow quantities for case 1**

| Variable | Vane-1 | Rotor-1 | Vane-2 | Rotor-2 |
|---|---|---|---|---|
| $M_{in}$ | 0.08 | 0.91 | 0.59 | 0.79 |
| $M_{out}$ | 1.17 | 0.85 | 1.09 | 0.81 |
| $P_{in}$, MPa | 15.33 | 4.15 | 3.89 | 2.07 |
| $P_{out}$, MPa | 4.15 | 3.89 | 2.07 | 1.75 |
| $Pt_{in}$, MPa | 15.40 | 7.79 | 4.97 | 3.16 |
| $Pt_{out}$, MPa | 11.10 | 6.36 | 4.35 | 2.83 |
| $Tt_{in}$, K | 1236 | 1111 | 1035 | 946 |
| $Tt_{out}$, K | 1235 | 1103 | 1029 | 944 |
| $\beta_{in}$, deg | 0.0 | 60.5 | −57.1 | 56.8 |
| $\beta_{out}$, deg | 63.8 | −70.1 | 67.4 | −55.2 |
| $W$, kJ/kg | — | 1149 | — | 970 |
| Reaction | — | 0.023 | — | 0.143 |
| $\eta_{tt-overall}$ | — | — | — | 0.621 |
| $\eta_{ts-overall}$ | — | — | — | 0.564 |

**Table 3 Turbine time-averaged relative flow quantities for case 2**

| Variable | Vane-1 | Rotor-1 | Vane-2 | Rotor-2 |
|---|---|---|---|---|
| $M_{in}$ | 0.08 | 0.90 | 0.59 | 0.79 |
| $M_{out}$ | 1.15 | 0.86 | 1.09 | 0.80 |
| $P_{in}$, MPa | 15.33 | 4.21 | 3.86 | 2.06 |
| $P_{out}$, MPa | 4.21 | 3.86 | 2.06 | 1.75 |
| $Pt_{in}$, Mpa | 15.40 | 7.74 | 4.95 | 3.14 |
| $Pt_{out}$, Mpa | 10.98 | 6.35 | 4.31 | 2.81 |
| $Tt_{in}$, K | 1236 | 1113 | 1036 | 948 |
| $Tt_{out}$, K | 1235 | 1105 | 1031 | 947 |
| $\beta_{in}$, deg | 0.0 | 59.2 | −56.5 | 56.8 |
| $\beta_{out}$, deg | 61.0 | −70.7 | 66.9 | −55.1 |
| $W$, kJ/kg | — | 1165 | — | 965 |
| Reaction | — | 0.031 | — | 0.147 |
| $\eta_{tt-overall}$ | — | — | — | 0.623 |
| $\eta_{ts-overall}$ | — | — | — | 0.568 |

**Table 4 Turbine time-averaged relative flow quantities for case 3**

| Variable | Vane-1 | Rotor-1 | Vane-2 | Rotor-2 |
|---|---|---|---|---|
| $M_{in}$ | 0.08 | 0.91 | 0.59 | 0.79 |
| $M_{out}$ | 1.15 | 0.86 | 1.08 | 0.85 |
| $P_{in}$, MPa | 15.33 | 4.12 | 3.82 | 2.07 |
| $P_{out}$, MPa | 4.12 | 3.82 | 2.07 | 1.75 |
| $Pt_{in}$, MPa | 15.40 | 7.67 | 4.90 | 3.12 |
| $Pt_{out}$, MPa | 10.87 | 6.35 | 4.29 | 2.80 |
| $Tt_{in}$, MPa | 1236 | 1113 | 1036 | 949 |
| $Tt_{out}$, MPa | 1235 | 1105 | 1032 | 947 |
| $\beta_{in}$, MPa | 0.0 | 59.1 | −57.3 | 56.7 |
| $\beta_{out}$, MPa | 60.0 | −70.7 | 67.5 | −55.3 |
| $W$, kJ/kg | — | 1116 | — | 986 |
| Reaction | — | 0.026 | — | 0.155 |
| $\eta_{tt-overall}$ | — | — | — | 0.609 |
| $\eta_{ts-overall}$ | — | — | — | 0.553 |

**Table 5 Turbine time-averaged relative flow quantities for case 4**

| Variable | Vane-1 | Rotor-1 | Vane-2 | Rotor-2 |
|---|---|---|---|---|
| $M_{in}$ | 0.08 | 1.07 | 0.59 | 0.80 |
| $M_{out}$ | 1.37 | 0.86 | 1.09 | 0.86 |
| $P_{in}$, MPa | 15.33 | 4.15 | 3.86 | 2.07 |
| $P_{out}$, MPa | 4.15 | 3.86 | 2.07 | 1.75 |
| $Pt_{in}$, MPa | 15.40 | 8.52 | 4.96 | 3.12 |
| $Pt_{out}$, MPa | 12.64 | 6.38 | 4.31 | 2.81 |
| $Tt_{in}$, K | 1236 | 1109 | 1035. | 948 |
| $Tt_{out}$, K | 1235 | 1105 | 1031. | 946 |
| $\beta_{in}$, deg | 0.0 | 72.7 | −57.3 | 56.8 |
| $\beta_{out}$, deg | 76.4 | −69.7 | 67.5 | −55.1 |
| $W$, kJ/kg | — | 1353. | — | 991 |
| Reaction | — | 0.025 | — | 0.151 |
| $\eta_{tt-overall}$ | — | — | — | 0.680 |
| $\eta_{ts-overall}$ | — | — | — | 0.618 |

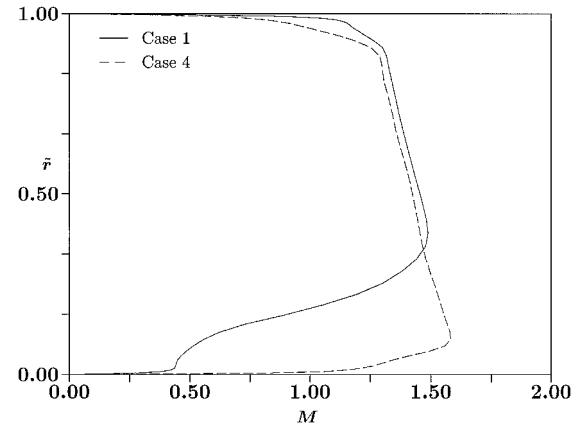


**Fig. 4 Absolute Mach-number profile: vane-1 exit.**

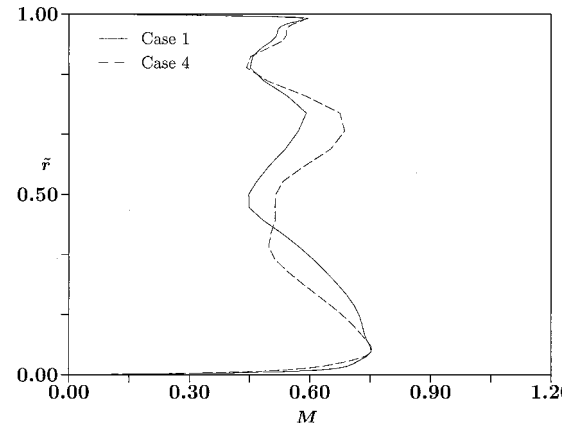


**Fig. 5 Absolute Mach-number profile: rotor-1 exit.**

3) The changes made to the first stage had little effect on the flow in the second stage.

4) The mass flow was the same in all four cases because the first-stage vane is choked and the throat area was held constant.

Time-averaged radial profiles of the absolute Mach number at the exit of the first-stage vane and rotor in cases 1 and 4 are shown in Figs. 4 and 5. The Mach-number profile at the exit of the first-stage vane (see Fig. 4) clearly shows the extent of the separated flow region. The flowfield begins to recover by the time it exits the first-stage rotor (see Fig. 5), and the Mach-number profiles were nearly identical in the second stage of the turbine. The presence of tip leakage flow is evident behind the rotor row (see Fig. 5).

## Conclusions

A set of unsteady three-dimensional Navier–Stokes simulations has been used to investigate the effects of end-wall shape and first-stage vane stacking on the performance of a two-stage supersonic

turbine. Restacking of the vanes was successfully used to eliminate a large separated/secondary flow region at the hub between the first-stage vanes and rotors. Altering the shape of the end wall in the first stage had little effect on the separated flow region. There was a significant performance increase obtained at the design flow conditions by reducing the separated flow region. It is anticipated that the benefits of improving the behavior of the flow near the end wall will be even greater at off-design operating conditions.

## Acknowledgments

The computer time for the flow simulations was provided by NASA Ames Research Center, Moffett Field, California. The authors are especially grateful to Chuck Niggley for assisting with the use of the computers.

## References

[1]Griffin, L. W., Dorney, D. J., Huber, F. W., Tran, K., Shyy, W., and Papila, N., "Detailed Aerodynamic Design Optimization of an RLV Turbine," AIAA Paper 2001-3397, July 2001.

[2]Papila, N., Shyy, W., Griffin, L. W., and Dorney, D. J., "Shape Optimization of Supersonic Turbines Using Response Surface and Neural Network Methods," AIAA Paper 2001-1065, Jan. 2001; *Journal of Propulsion and Power*, Vol. 18, No. 3, 2002, pp. 509–518.

[3]Griffin, L. W., and Dorney, D. J., "RLV Turbine Performance Optimization," Pennsylvania State Univ., PERC 12th Symposium on Propulsion, Oct. 2000.

[4]Dorney, D. J., Griffin, L. W., and Huber, F., "A Study of the Effects of Tip Clearance in a Supersonic Turbine," *Journal of Turbomachinery*, Vol. 122, No. 4, 2000, pp. 664–673.

[5]Dorney, D. J., Griffin, L. W., Huber, F., and Sondak, D. L., "Unsteady Flow in a Supersonic Turbine Stage with Variable Specific Heats," AIAA Paper 2001-3884, July 2001; *Journal of Propulsion and Power*, Vol. 18, No. 2, 2002, pp. 493–496.

# Controlling Electron Backstreaming Phenomena Through the Use of a Transverse Magnetic Field

John E. Foster* and Michael J. Patterson†
*NASA John H. Glenn Research Center at Lewis Field, Cleveland, Ohio 44135*

## Nomenclature

| | | |
|---|---|---|
| $B$ | = | magnetic field |
| $D_\perp$ | = | cross-field electron diffusion coefficient |
| $D_e$ | = | field-free electron diffusion coefficient |
| $E_s$ | = | electric field |
| $e$ | = | elementary charge of an electron |
| $J_{\text{beam}}$ | = | ion beam current |
| $J_e$ | = | electron cross-field current density |
| $J_{\text{limit}}$ | = | Measured ion beam current at backstreaming limit |
| $k$ | = | Boltzmann's constant |
| $m$ | = | mass of electron |
| $n_e$ | = | electron number density |
| $r$ | = | displacement normal to field line direction |
| $T_e$ | = | electron temperature |
| $\lvert V_a \rvert$ | = | absolute value of accelerator grid voltage |
| $\nu_e$ | = | electron collision frequency |
| $\mu_e$ | = | electron mobility |
| $\omega$ | = | electron cyclotron frequency |

Received 1 April 2002; revision received 12 June 2002; accepted for publication 5 August 2002. 

*Research Scientist, On-Board Propulsion and Power Group, MS 301-3, 21000 Brookpark Road. Member AIAA.

†Aerospace Engineer. Member AIAA.

## Introduction

DEEP-SPACE mission propulsion requirements can be satisfied by the use of high specific impulse systems such as ion thrusters. For such missions, however, the ion thruster will be required to provide thrust for long periods of time. To meet the long operation time and high-propellant throughput requirements, thruster lifetime must be increased. In general, potential ion thruster failure mechanisms associated with long-duration thrusting can be grouped into four areas[1,2]: 1) ion optics failure, 2) discharge cathode failure 3) neutralizer failure, and 4) electron backstreaming caused by accelerator grid aperture enlargement brought on by accelerator grid erosion. The work presented here focuses on electron backstreaming, which occurs when the potential at the center of an accelerator grid aperture is insufficient to prevent the backflow of electrons into the ion thruster. The likelihood of this occurring depends on ion source operation time, plasma density, and grid voltages, as accelerator grid apertures enlarge as a result of erosion. Electrons that enter the gap between the high-voltage screen and accelerator grids are accelerated to the energies approximately equal to the beam voltage. This energetic electron beam (typically higher than 1 kV) can damage not only the ion source discharge cathode assembly, but also any of the discharge surfaces upstream of the ion acceleration optics that the electrons happen to impact. Indeed, past backstreaming studies have shown that near the backstreaming limit, which corresponds to the absolute value of the accelerator grid voltage below which electrons can backflow into the thruster, there is a rather sharp rise in temperature at structures such as the cathode keeper electrode (Soulas, G. C., and Rawlin, V. K., private communication, NASA Glenn Research Center, Cleveland, OH, Feb. 2001). In this respect operation at accelerator grid voltages near the backstreaming limit is avoided.

Generally speaking, electron backstreaming is prevented by operating the accelerator grid at a sufficiently negative voltage to ensure a sufficiently negative aperture center potential. This approach can provide the necessary margin assuming an expected aperture enlargement. Operation at very negative accelerator grid voltages, however, enhances ion charge-exchange and direct impingement erosion of the accelerator grid.

The focus of the work presented here is the mitigation of electron backstreaming by the use of a magnetic field. The presence of a magnetic field oriented perpendicular to the thruster axis can significantly decrease the magnitude of the backflowing electron current by significantly reducing the electron diffusion coefficient. Negative ion sources utilize this principle to reduce the fraction of electrons in the negative ion beam.[3–7] The focus of these efforts has been on the attenuation of electron current diffusing from the discharge plasma into the negative ion extraction optics by placing the transverse magnetic field upstream of the extraction electrodes. In contrast, in the case of positive ion sources such as ion thrusters, the approach taken in the work presented here is to apply the transverse field *downstream* of the ion extraction system so as to prevent electrons from flowing back into the source. It was found in the work presented here that the magnetic field also reduces the absolute value of the electron backstreaming limit voltage. In this respect, the applied transverse magnetic field provides two mechanisms for electron backstreaming mitigation: 1) electron current attenuation and 2) backstreaming limit voltage shift. Such a shift to less negative voltages can lead to reduced accelerator grid erosion rates.

## Conceptual Basis

In general, the diffusion of electrons across a magnetic field can be described by[8]

$$J_e = -e \cdot \mu_e \cdot n_{e\cdot} \cdot E_s - e \cdot D_\perp \cdot \frac{\mathrm{d}n_e}{\mathrm{d}r} \tag{1}$$